RSC Advances

PAPER

View Article Online
View Journal | View Issue

Cite this: *RSC Adv.*, 2023, **13**, 23050

Surface-decorated porphyrinic zirconium-based metal–organic frameworks (MOFs) using post-synthetic self-assembly for photodegradation of methyl orange dye†

Ahmed M. Kobaisy,[a] Marwa F. Elkady,[b] Ahmed A. Abdel-Moneim[a] and Mohamed E. El-Khouly *[a]

We report herein the surface decoration of a water-soluble free-base porphyrin, namely, 5,10,15,20-tetrakis(1-methyl-4-pyridinio)porphyrin-tetra(*p*-toluenesulfonate) (H_2TMPyP), over three different zirconium-based metal–organic frameworks of different linker structure and functionality; namely UiO66, UiO66-NH_2, and MIP-202, *via* self-assembly. The synthesized MOFs along with the resulting complexes have been characterized *via* spectroscopic and analytical techniques (XRD, FT-IR, TEM, N_2 adsorption/desorption, and laser scanning confocal microscopy). The self-assembly of H_2TMPyP with the examined three MOFs was observed by using the steady-state absorption and fluorescence, as well as the fluorescence lifetime studies. It was evident that the highest complex interaction was recorded between porphyrin and UiO-66-NH_2 compared with the lowest interactions between porphyrin and MIP-202. This is in good agreement with the high surface area and pore volume of UiO-66 (1100 $m^2\ g^{-1}$ and 0.68 $cm^3\ g^{-1}$) and compared to that of MIP-202 (94 $m^2\ g^{-1}$ and 0.26 $cm^3\ g^{-1}$). The photocatalytic activities of the three porphyrin entities immobilized zirconium-based MOFs were compared toward methyl orange dye degradation from aqueous solution under visible light irradiation (λ_{ex} = 430 nm). The photocatalytic studies render the fabrication of the self-assembled H_2TMPyP@UiO-66-NH_2 composite as a promising material for dye degradation from polluted wastewater.

Received 21st April 2023
Accepted 22nd July 2023

DOI: 10.1039/d3ra02656f

rsc.li/rsc-advances

1. Introduction

During the last few decades, heterogeneous photocatalysis has emerged as one of the most interesting research topics. It has been used for generating solar fuels, water treatment, and nitrogen gas reduction.[1] The typical photocatalytic process can be subdivided into three main stages: light absorption, charge separation forming an exciton, and interaction of the charge with a substrate.[2]

Metal–organic frameworks (MOFs) are among the most promising candidates as heterogeneous photocatalysts.[3,4] MOFs used in photocatalysis are classified into three main types. In type I MOFs, the metallic clusters (SBUs) are regarded as 0D semiconductors, while the organic linker molecules are considered spacers that separate them throughout the MOF crystal. Type II MOFs, on the other hand, have functional dyes as organic linkers linked together in ordered and organized arrays in the MOF crystal using metallic nodes. In type III MOFs, the photocatalytic species (the organic dye in our case) of suitable size is encapsulated inside the MOF pores *via in situ* preparation[5,6] Another way to form type III MOF photocatalysts is by soaking the MOF of suitable binding sites in a dye solution.[7] This method does not give the maximum loading capacity unless the pore size, volume, and binding sites of the MOF are suitable for the guest dye molecule, but it is still much more straightforward than the *in situ* method. Although this method is much less complex than the previous method, it gives much fewer loading percentages than the *in situ* preparation.

Porphyrins are well-known for their outstanding optical properties; thus, they are used as photocatalysts[8,9] solar energy conversion[10,11] and biomedical applications.[12,13] The synthesis of porphyrin-based metal–organic framework complexes and their utilization as light-harvesting materials was extensively investigated in the literature.[14] One way to load porphyrins on metal–organic frameworks is by *in situ* preparation. Eddaoudi *et al.* managed for the first time to encapsulate H_2TMPyP in the pores of the strongly anionic rho-ZMOF by *in situ* preparation.[15] The resulting "ship in a bottle" structure of H_2TMPyP inside the MOF cavities could be achieved due to the meticulous design of

[a]*Nanoscience Program, Institute of Basic and Applied Science, Egypt-Japan University of Science and Technology (E-JUST), New Borg El-Arab City, Alexandria, Egypt. E-mail: mohamed.elkhouly@ejust.edu.eg*

[b]*Chemical and Petrochemicals Engineering Department, Egypt-Japan University of Science and Technology (E-JUST), New Borg El-Arab City, Alexandria, Egypt*

† Electronic supplementary information (ESI) available. See DOI: https://doi.org/10.1039/d3ra02656f

MOF of large pore size along with small pores around the MOF cavities to prevent leaching. Although this technique can produce significantly higher porphyrin loading percentages in the resulting complex, it is unsuitable for all MOFs.

Another way to add porphyrin to the MOF structure is *via* post-synthetic self-assembly. Rabiee *et al.* introduced porphyrins post-synthetically to the surface of NH_2-MIL-53 by mixing it with leaf extracts to enhance its sensitivity for the detection of ultra-trace concentrations of ssDNA, sgRNA, anti-cas9 proteins, and recombinant SARS-CoV-2 spike antigen.[16] Moreover, Kan *et al.* used a similar technique by mixing UiO-66 with TPP-SH in CH_2Cl_2 for several hours at room temperature to obtain a surface-decorated porphyrinic metal–organic framework, which proved its efficiency as a PDT agent.[17] This method produces lower yields than the *in situ* method. However, this method is easier to apply and provides more accessibility to the porphyrin molecules.

Using post-synthetic self-assembly in DMF, Wang *et al.* examined the DOPA functionalization of three isoreticular, unfunctionalized Zr-based MOFs with various linker lengths (UiO-66, UiO-67, and BUT-30).[18] This technique was employed to alter the nanoMOF surface chemistry while preserving crystallinity and permanent porosity by coordinating to exposed metal-containing units.

Herein, we investigate the post-synthetic surface decoration of a free-base tetra cationic porphyrin (H_2TMPyP) with three synthesized zirconium-based metal–organic frameworks possessing different linkers; terephthalic acid for UiO-66, 2-aminoterepthalic acid for the amine-functionalized UiO-66, and aspartic acid for MIP-202. The selection of the three linkers is based on targeting different potential modes of interaction with the tetra cationic porphyrin, and thus varying the loading of the porphyrin on the selected MOFs (Scheme 1). The photocatalytic activity of the three complexes was also evaluated for Methylene orange (MO), and Methyl orange (MO) degradation in aqueous media using a continuous-flow photoreactor under visible light.

2. Materials and methods

2.1. Chemicals and materials

All reagents and chemicals were of the best available analytical reagent and were used as received without purification. Deionized H_2O was obtained from a US Filter Corporation deionization system. 5,10,15,20-Tetrakis(1-methyl-4-pyridinio) porphyrin-tetra(*p*-toluenesulfonate) (H_2TMPyP) was purchased from (TCI-Ace, JAPAN). Zirconium tetrachloride ($ZrCl_4$) was purchased from Acros Organics, 1,4-benzenedicarboxylic acid (BDC), and 2-aminobenzene-1,4-dicarboxylic acid (BDC-NH_2) were purchased from Sigma-Aldrich. All the measurements were performed at room temperature and under atmospheric pressure. Quartz cuvettes with a 1.00 cm path length were used for all measurements.

2.2. Synthesis of zirconium-based MOFs

2.2.1. Synthesis of UiO-66. UiO-66 was synthesized *via* the conventional solvothermal method shown in Scheme 2. Briefly, in a 100 mL screw-top bottle, 1,4-benzenedicarboxylic acid (BDC) (0.83 g), zirconium tetrachloride $ZrCl_4$ (1.17 g), and 37% HCl (0.8 mL) were mixed and sonicated in 30 mL of DMF

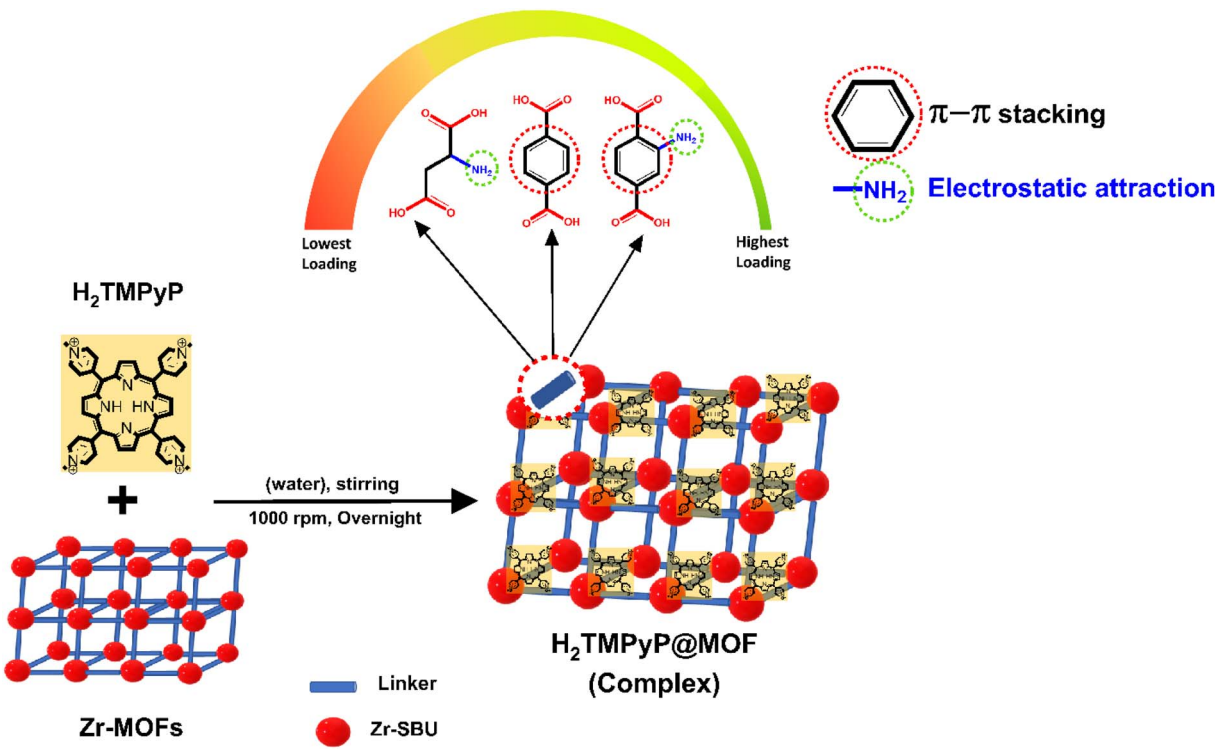

Scheme 1 Schematic representation of the building blocks of the three MOFs and their targeted non-covalent interactions with H_2TMPyP.

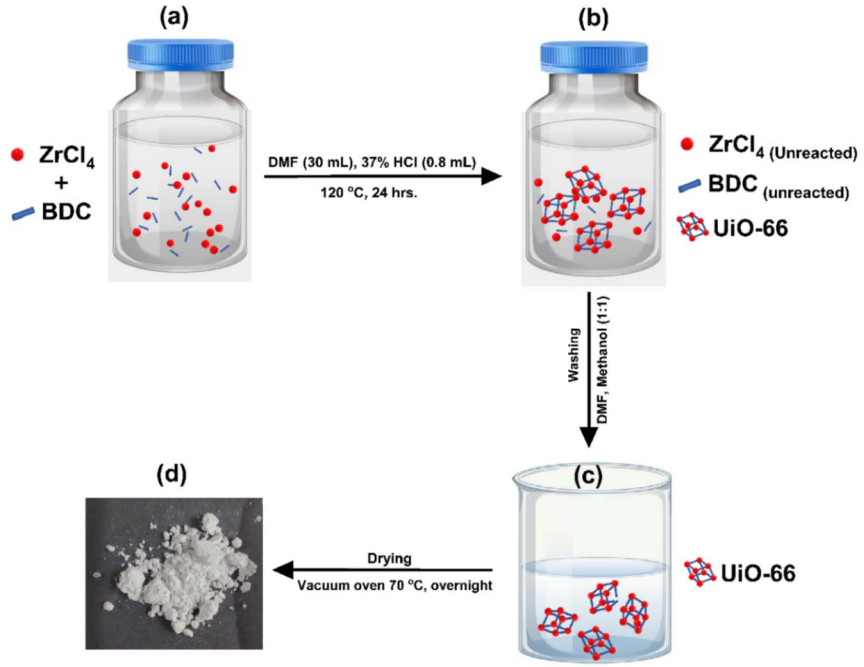

Scheme 2 Schematic representation of the general procedure of synthesizing UiO-66 using a conventional solvothermal technique.

for 20 minutes, then heated in the oven for 24 h at 120 °C. The resulting MOF was cooled to room temperature, centrifuged for 15 minutes at 6000 rpm, and washed several times using (1 : 1) mixed reagent of DMF and anhydrous methanol. The resulting UiO-66 was activated in a vacuum oven at 100 °C overnight.

2.2.2. Synthesis of UiO-66-NH_2. Similarly, the amine-functionalized UiO-66 was synthesized UiO-66 was synthesized. Briefly, in a 100 mL screw-top bottle, 2-aminobenzene-1,4-dicarboxylic acid (BDC-NH_2) (0.27 g), zirconium tetrachloride $ZrCl_4$ (0.25 g), and 37% HCl (0.8 mL) were mixed and sonicated in 30 mL of DMF for 20 minutes, then heated in the oven for 24 h at 120 °C. The resulting MOF was cooled to room temperature, centrifuged for 15 minutes at 6000 rpm, and washed several times using (1 : 1) mixed reagent of DMF and anhydrous methanol. The resulting UiO-66 was activated in a vacuum oven at 100 °C overnight.

2.2.3. Synthesis of MIP-202. MIP-202 was synthesized according to the green hydrothermal procedure made by Diab *et al.*[19] In a 100 mL beaker, Aspartic acid (2.8 g) was dispersed in 10 mL of deionized water using ultrasonication for 10 minutes. On the other hand, zirconium tetrachloride $ZrCl_4$ (2.3 g) was mixed and sonicated in 10 mL of deionized water for 30 minutes. The $ZrCl_4$ solution was then added to the aspartic acid solution dropwise under sonication. The mixture was then transferred to a reflux system and heated for 24 hours at 100 °C under magnetic stirring at 500 rpm. The resulting MOF was cooled to room temperature, centrifuged for 15–20 minutes at 6000 rpm, washed several times with water and ethanol, and dried in a vacuum oven at 60 °C overnight.

2.2.4. Synthesis of MOF@H_2TMPyP composites. All the MOF@dye composites were synthesized using the same procedure followed by Xie *et al.*[7] The MOFs were soaked in a concentrated aqueous solution of H_2TMPyP and stirred overnight at 1000 rpm to achieve maximum H_2TMPyP loading. The resulting complex was washed with deionized water multiple times, centrifuged at 9000 rpm for 3 minutes, and dried in a vacuum oven at 70 °C overnight.

2.3. Characterization techniques

In order to confirm the crystallographic structures of the three prepared zirconium-based MOFs, X-ray diffraction (Shimadzu-X-lab 600, Japan) was carried out at 40 kV with Cu Kα radiation. Steady-state absorption and fluorescence spectra were recorded using a UV-vis spectrophotometer (Shimadzu UV-2600) and spectrofluorometer (Shimadzu RF-6000), respectively. Laser microscopy measurements were performed on MOF films prepared using drop casting on a glass substrate using a Keyence 3D laser microscope. Transmission electron microscopy (TEM) images were captured using a JEOL 2100 microscope operating at an accelerating voltage of 200 kV. The information on functional groups of the prepared materials was determined using FTIR (Shimadzu 8400s, Japan).

2.4. Photocatalytic activity of porphyrin@MOF complexes toward methyl orange dye degradation in aqueous solution

The three fabricated MOF composites were compared against their potential photocatalytic degradation of methyl orange dye under visible light irradiation (λ_{ex} = 430 nm). The photocatalytic experiment was conducted using a continuous-flow reactor (Vapour tech. UV-150) at room temperature (25 °C), keeping a constant flow rate of (5 mL min^{-1}), and a constant catalyst dose of 10 mg per 100 mL of the dye solution. The

working procedure is similar to the procedure previously discussed by Safo *et al.*[20] Each catalyst sample was added to a 100 mL dye solution (20 ppm) under stirring without adding any buffers. The samples were kept in the dark for 60 minutes in order to reach the adsorption–desorption equilibrium. After that, the samples were subjected to the LED lamp irradiation ($\lambda_{ex} = 430$ nm) in the (UV-150) reactor for additional 60 minutes, at which the product was collected every 10 minutes, centrifuged for 5 minutes at 7000 rpm to remove any dispersed catalyst, and decanted. The absorbance of the supernatant at 464 nm was determined using a spectrophotometer to detect the photodegradation of the dye. The photocatalytic degradation efficiency was evaluated according to the following equation:

$$\eta_{deg} = (\Delta A)/A_0 \times 100$$

where (η_{deg}) stands for the photocatalytic degradation efficiency, (A_0) indicates the initial absorbance, and (ΔA) stands for the difference between initial absorbance and absorbance at a given time.

3. Results and discussion

3.1. Characterization of MOFs and MOF complexes

All the MOF@dye composites were synthesized using the same procedure followed by Xie *et al.*[21] The MOFs were soaked in a concentrated aqueous solution of H_2TMPyP and stirred overnight at 1000 rpm to achieve maximum H_2TMPyP loading. The resulting complex was washed with deionized water multiple times, centrifuged at 9000 rpm for 3 minutes, and dried in a vacuum oven at 70 °C overnight. The loading efficiency (η) of the H_2TMPyP was calculated by the following equation:[22]

$$\eta = \frac{m_0 - m_s}{m_{MOF}}$$

where m_0 is the mass of the dye in the initial dye solution, m_s is the mass of H_2TMPyP in the supernatant after loading, and m_{MOF} is the mass of the MOF. The m_s value was determined by fitting the absorbance value of the supernatant on the calibration curve of H_2TMPyP at $\lambda = 520$ nm (Fig. S1†). According to this method, the porphyrin loading efficiency on the surface of the MOFs was found to be the lowest in the case of MIP-202 ($\eta =$ 0.09%), the loading efficiency increased to 0.15% in the case of UiO-66, while UiO-66-NH_2 achieved the highest loading efficiency with ($\eta = 0.21\%$), which is more than the double of MIP-202. The stability of the resulting complexes using UV-vis spectroscopy in aqueous media has been tested for 18 hours and they were found to be stable under ambient conditions of temperature and pH. Also, the three normalized absorption spectra of the three complexes shown in Fig. S10† show the presence of the porphyrin peak at 425 nm, which confirms the loading of the porphyrin on the MOF.

3.1.1. XRD. As previously mentioned, three zirconium-based metal–organic frameworks were synthesized namely, UiO-66, UiO-66-NH_2, and MIP 202. As shown in Fig. 1, the XRD

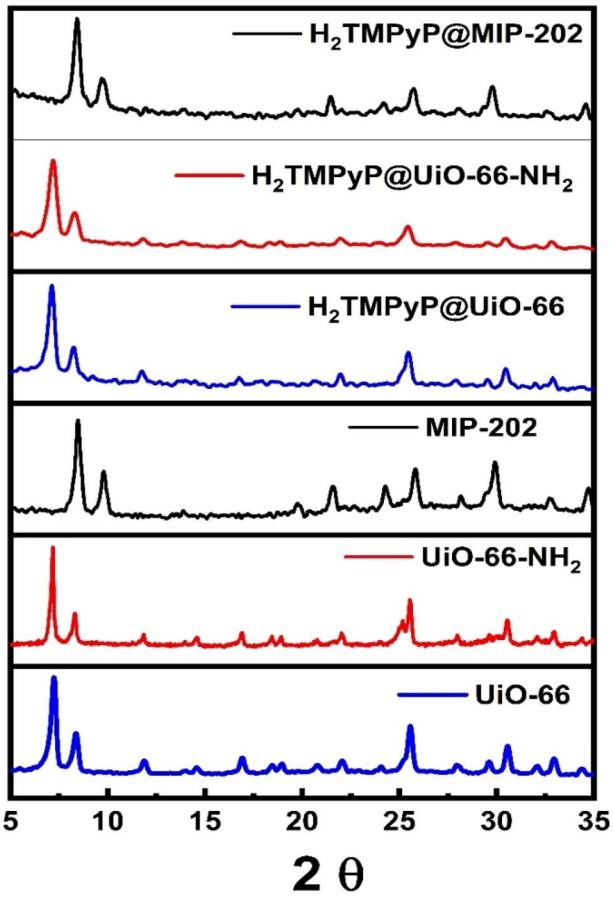

Fig. 1 XRD of the synthesized UiO-66, UiO-66-NH_2, and MIP-202.

data exhibited three significant peaks in the case of UiO-66 at 7.24°, 8.38°, and 25.56°. UiO-66-NH_2 also has three identified peaks at 7.19°, 8.31°, and 25.55° with a sharp shoulder at 25.18° corresponding to the (111), (002), and (006) planes respectively. These results are in good agreement with the values in the literature.[16] On the other hand, MIP-202 has distinguishable peaks at 8.84°, 9.84°, 19.78° and 21.56° corresponding to the (111), (200), (420), and (440) planes as previously investigated in the literature. Accordingly, XRD patterns confirm the successful preparation of the three zirconium-based metal–organic frameworks. Although the XRD data shown in Fig. 1 did not exhibit a significant change in the PXRD patterns after immobilization of the three MOF types with H_2TMPyP, it may prove that the MOF's crystallinity was preserved before and after adding the porphyrin.

3.1.2. HR-TEM. High-resolution transmission electron microscopy (HR-TEM) was used to confirm the self-assembly between the porphyrin and synthesized zirconium-based MOFs. The TEM images in Fig. 2a–c reveal the aggregation of MOF particles as a result of the complex formation between H_2TMPyP and the three MOF types. The highest aggregation is observed in the UiO-66-NH_2 complex, and the lowest level of aggregation is observed in the MIP-202 complex. These results suggested that the interactions between the porphyrin dye and UiO-66-NH_2 are higher than that between the porphyrin dye and MIP-202.

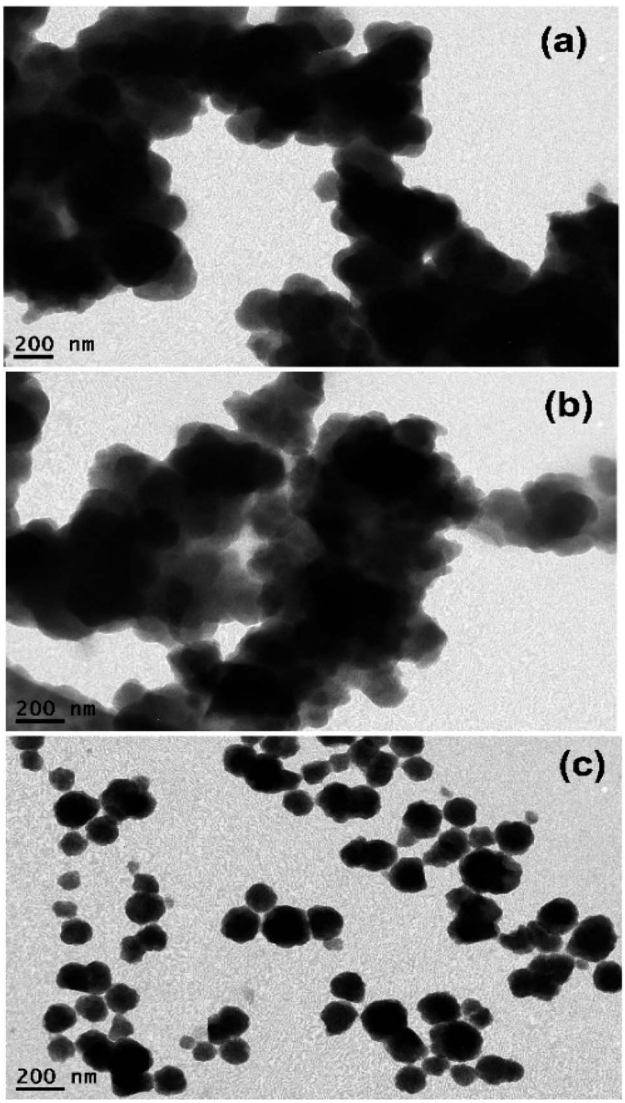

Fig. 2 HR-TEM images of (a) H_2TMPyP@UiO-66-NH_2 complex, (b) H_2TMPyP@UiO-66 complex, and (c) H_2TMPyP@MIP-202 complex.

In order to confirm the loading of H_2TMPyP on the MOFs, TEM-EDS elemental analysis was performed for the pristine MOFs as well as the three MOF complexes (Fig. S2–S7†). The nitrogen peaks could not be detected in the TEM-EDS spectra due to their overlapping with carbon and oxygen peaks. However, the presence of nitrogen in the sample could be detected from elemental mapping. The presence of sulfur, which is only present in H_2TMPyP in the complex samples in very small amounts as well as the increasing carbon ratio in H_2TMPyP@UiO-66-NH_2 and H_2TMPyP@UiO-66 samples can confirm the porphyrin loading on the MOFs. The carbon ratio in the H_2TMPyP@MIP-202 slight decrease compared to the MIP-202 sample along with the unexpected increase in the sulfur ratio may suggest that the linker exchange mechanism can be favorable in the case of MIP-202. Overall, the EDS mapping reveals uniform and homogenous distributions of the elements in the three MOF complexes, including C, O, N, S, and Zr along the surfaces.

3.1.3. BET. The nitrogen adsorption–desorption isotherms of UiO-66 and MIP-202 were studied to gain insight into their surface area and pore volume. This important information helps to understand the physical characteristics of the material, which are crucial for determining its suitability for various applications. The results of the nitrogen adsorption–desorption isotherms showed the amount of nitrogen adsorbed by the UiO-66 and MIP-202 samples as a function of pressure. From these measurements, the BET surface area and pore volume of UiO-66 were determined to be 1100 $m^2\ g^{-1}$ and 0.6834 $cm^3\ g^{-1}$, respectively. It is noteworthy to mention that this surface area is comparable and matches the surface area reported for UiO-66 MOF.[23] As a result, one favorable probability for the H_2TMPyP molecules to assemble on the surface of the UiO-66 as it offers a large space for adsorption, as both the high surface area and pore volume provide ample space for the H_2TMPyP molecules to be adsorbed inside the pores of H_2TMPyP.[16,21] Also, there is a probability for the diffusion of the porphyrin molecules by linker exchange as reported in the literature.[24,25] However, the nitrogen adsorption–desorption isotherms of the complexes

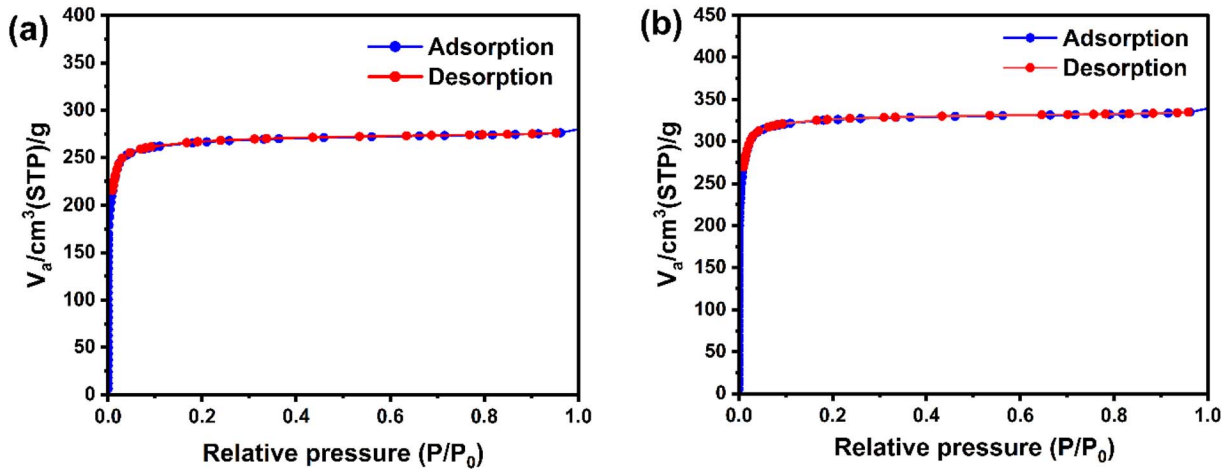

Fig. 3 N_2 adsorption–desorption isotherms of (a) H_2TMPyP@UiO-66-NH_2, and (b) H_2TMPyP@UiO-66.

(Fig. 3) show surface area values of 835 and 996 $m^2\ g^{-1}$ and pore volume values of 0.4317 and 0.5230 $cm^3\ g^{-1}$ for the H_2-TMPyP@UiO-66-NH_2 and H_2TMPyP@UiO-66 complexes, respectively. This slight decrease in the surface area can be explained in terms of the successful porphyrin loading on the MOF. The surface area and pore volume of MIP-202 bio-MOF were also determined to be around 94 $m^2\ g^{-1}$ and 0.26 $cm^3\ g^{-1}$, respectively. It is noteworthy to mention that the N_2 isotherm and surface area values are consistent with previous reports of the MIP-202 bio-MOF and that the resulting porosity is attributed to the shrinking of the MOF micropores towards the nitrogen.[16]

3.1.4. FT-IR. The FTIR spectra obtained from H_2TMPyP, Zr-MOFs, and their complexes are shown in Fig. 5. Revealing spectral changes before and after the surface decoration with H_2TMPyP. The spectrum of H_2TMPyP exhibits fingerprint bands attributed to the amino groups present in the structure of the macrocycle and the pyridinium groups at 681, 733, 807, 1008, 1033, 1565, and 1641 cm^{-1}, corresponding to in-plane vibration deformation porphyrin, out-of-plane N–H bending, out-of-plane C–H bending, C–H rocking vibrations, in-plane N–H bending and C=C stretch vibrations, respectively.[26,27] On the other hand, the FT-IR spectrum of UiO-66-NH_2 (Fig. 4a) exhibited a strong peak at 1657 cm^{-1}, which can be related to the ν(C=O) stretching of *N*,*N*-dimethylformamide (DMF). The absence of this band in the complex indicates the complete exchange of DMF with water.[28,29] The 3000–2800, and 3600–3100 cm^{-1} bands are assigned to the stretching vibration of CH_2 and unreacted amino groups, respectively. However, the fact that these signals became slightly stronger after the addition of H_2TMPyP can be attributed to the successful incorporation of the H_2TMPyP on the MOF surface.[28] The characteristic stretching vibration peaks of NH_2 on the MOF appeared at 1435 and 1256 cm^{-1}. Another band at 1622 cm^{-1} can be attributed to the N=C bond (stretching vibration).[28,30]

Likewise, UiO-66 exhibited a (C=O) stretching peak arising from DMF residues at 1655 cm^{-1}, which diminishes clearly in the complex (Fig. 4b). The MIP-202 (Fig. 4c) has a characteristic peak at 3447 cm^{-1} corresponding to the symmetric and asymmetric vibrations of the NH_2 group of the aspartate linker. This peak became sharper in the case of H_2TMPyP@MIP-202 due to the interference with the sharp porphyrinic peak at 3419 cm^{-1} indicating successful loading of the porphyrins. Moreover, the presence of two other peaks can be noticed at 2924 and 2851 cm^{-1} corresponding to the symmetrical and asymmetrical stretching vibration of methylene groups (CH_2) in the aspartate linker. The characteristic double peak of MIP-202 in the range between 1400–1600 cm^{-1} can be attributed to the symmetric stretching vibration of the carboxylate group in the amino acid.

3.2. Spectroscopic studies for the self-assembly complexes

3.2.1. UV-vis spectroscopy. UV-vis absorption spectra of H_2TMPyP in aqueous media (Fig. S8†) show a conventional sharp Soret band resulting from the ($S_0 \rightarrow S_2$) transition at around 422 nm. This band undergoes a slight blue shift upon increasing the concentration of H_2TMPyP from 0.25 to 2.91 μM to become 423.5 nm. Also, Q-band resulting from the ($S_0 \rightarrow S_1$) transition can be observed at around 520 nm. Photometric titrations have been conducted on H_2TMPyP using multiple additions of three Zr-based MOFs, namely UiO-66-NH_2, UiO-66, and MIP-202. Before the addition of UiO-66-NH_2, H_2TMPyP has shown a main sharp absorption band at 422 nm and another smaller absorption band at 519 nm. Upon titration with UiO-66-NH_2 (Fig. 5a), we could notice a significant decrease in the absorbance intensity accompanied by an 8 nm red shift of the main band to reach 430 nm with two clear isosbestic points at 411 and 431 nm. Similar behavior was recorded upon the addition of UiO-66 and MIP-202 to the aqueous solutions of H_2TMPyP (Fig. 5b and c). This decrease of the absorbance along with the red shift suggests the self-assembly of H_2TMPyP over the surface of the examined types of MOFs (UiO-66-NH_2, UiO-66, and MIP-202) through different binding modes. Based on the Benesi–Hildebrand method shown in Fig. 5d,[31] the binding constants (K_b) for the Zr-based MOF complexes with H_2TMPyP were calculated in the following order: $1.13 \times 10^5\ M^{-1}$ (for UiO-66-NH_2), $4.89 \times 10^4\ M^{-1}$ (for non-functionalized UiO-66), while the MIP-202 possessed the lowest binding constant ($K_b = 3.19 \times 10^4\ M^{-1}$). Implying that the dominant mode of interaction during the formation of the H_2TMPyP@UiO66 complex is π–π stacking, while in the case of H_2TMPyP@UiO66-NH_2 hydrogen bonding between the pyridinium ring of the porphyrin and the amine group of the MOF may lead to added stability to the formed complex along with π–π stacking.

3.2.2. Steady-state and time-resolved fluorescence measurements. The fluorescence spectrum of H_2TMPyP in an aqueous medium exhibited a broad emission band at 658.5 nm,

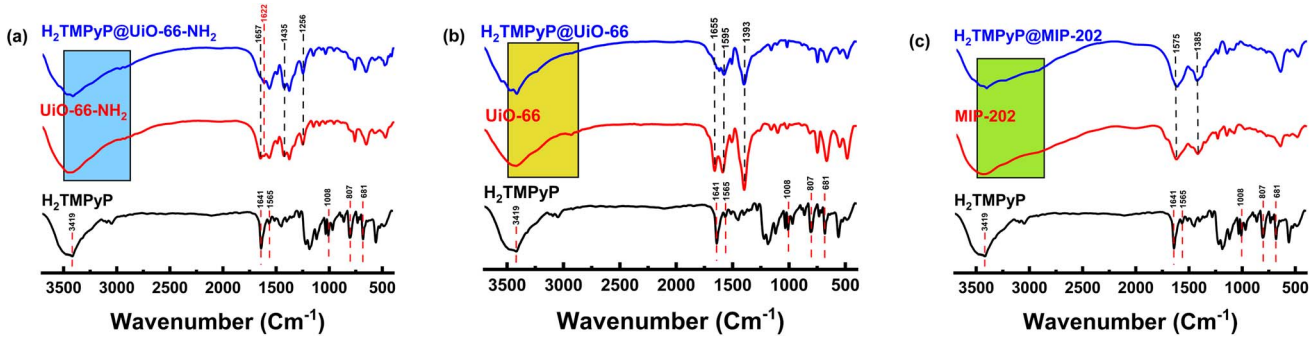

Fig. 4 FT-IR spectra of H_2TMPyP (black), Zr-based MOFs (red), and MOF@H_2TMPyP complexes (blue).

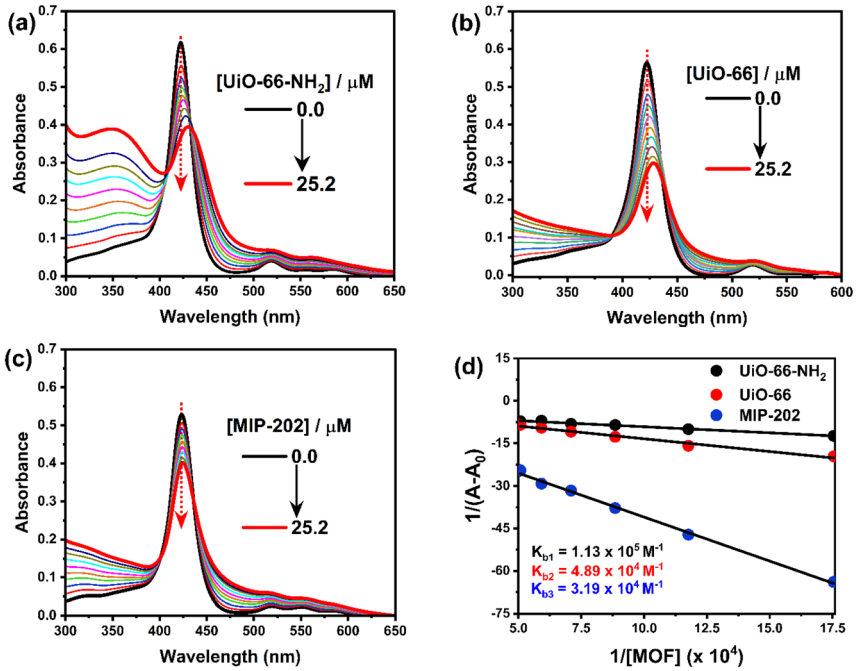

Fig. 5 UV-vis absorption spectra of photometric titration of H_2TMPyP (3.0 μM) in the presence of: (a) UiO-66, (b) UiO-66-NH_2, (c) MIP-202, (d) Benesi–Hildebrand plot for the three titrations to determine the binding constant K_b.

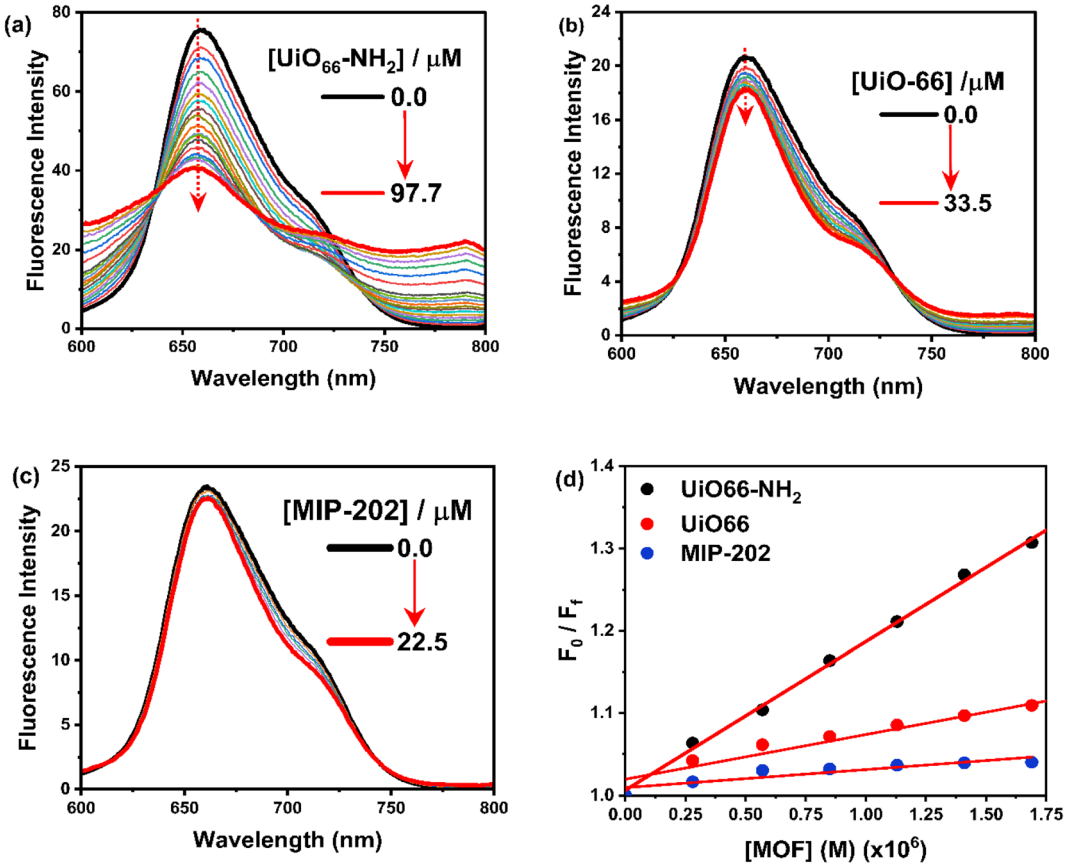

Fig. 6 Fluorescence spectra for titration of H_2TMPyP (3.0 μM) of H_2TMPyP (3.0 μM) in the presence of (a) UiO-66, (b) UiO-66-NH_2, (c) MIP-202. The concentrations of MOFs were kept at (0–25.2 μM). (d) Stern–Volmer plots.

from which the energy of the singlet excited state was calculated to be 1.88 eV (Fig. 6a).[32] By adding further various amounts of UiO-66-NH_2 to a solution of H_2TMPyP, a significant fluorescence quenching of the emission band of H_2TMPyP was observed accompanied by a considerable red-shift (≈3 nm), and the appearance of a new weak emission band at 790 nm. Similarly, the fluorescence quenching of H_2TMPyP was observed in the presence of UiO-66 and MIP-202 (Fig. 6b and c). Similarly, upon titration using UiO-66, we could notice a 6.5 nm red shift in the main band with two isosbestic points at 410, and 429 nm (Fig. 6b). The emission spectra (Fig. 6b) show noticeable fluorescence quenching. Also, the vibrational resolution of the shoulder increased. After adding MIP-202 (Fig. 6c), we could notice the formation of two isosbestic points at 613, and 744 nm along with slight emission quenching of H_2TMPyP with a non-significant red shift (≈1 nm). Similar behavior concerning the bathochromic shifting of the H_2TMPyP Soret band was explained in the literature in terms of the flattening of the porphyrin rings on the surface due to π–π stacking during its self-assembly with the negatively charged chemically converted graphene (CCG)[33] and LAPONITE®[34] which suggests that the red-shifting can arise from the porphyrin ring flattening. Moreover, the formation of a stable isosbestic point after several additions of the three MOFs eliminates the possibility of any contribution of J-aggregates formation to this bathochromic shift.[33,34] Based on the Stern–Volmer plots shown in Fig. 6d, it is apparent that the rate constants of the self-assembly process decrease were found to be in the order of UiO-66-NH_2 (1.8×10^4 L M^{-1}) > UiO-66 (5.4×10^3 L M^{-1}) > MIP-202 (2.2×10^3 L M^{-1}).[35]

The fluorescence lifetime measurements were also performed to track the steady-state fluorescence measurements in a quantitative way using 439 nm excitation light (Fig. 7 and S9†). The decay profile of H_2TMPyP could be fitted as a single-exponential decay, where the fluorescence lifetime (τ_0) of H_2TMPyP was found to be 2.75 ns. Upon adding UiO-66-NH_2, we could observe a gradual formation of a bi-exponential process with gradual quenching in fluorescence lifetime. At the end of the titration, the addition of 97.7 μM of UiO66-NH_2 resulted in a fast decay component (τ_1) with a lifetime of 0.3 ns and a slow decay component (τ_2) with a lifetime of 1.9 ns. On the other hand, upon adding 87.3 μM of UiO-66 a bi-exponential decay profile becomes clear with a relatively faster decay component (τ_1) with a lifetime of 0.5 ns, and a slower decay component (τ_2) with a lifetime of 4.3 ns. Upon adding 49.9 μM of UiO-66, a bi-exponential decay profile becomes clear with a relatively faster decay component (τ_1) with a lifetime of 1.6 ns.

3.2.3. Laser scanning confocal microscopy. The use of laser scanning confocal microscopy provided additional evidence for the H2TMPyP's successful self-assembly with the three Zr-MOFs under examination. Fig. 8a depicts the image of the UiO-66-NH_2 under examination, while Fig. 8b depicts the image of the H_2-TMPyP@UiO-66-NH_2 that was self-assembled. As can be seen, the brightness exhibited in the case of H_2TMPyP@UiO-66-NH_2 would indicate that H_2TMPyP units were successfully loaded onto the surface of UiO-66-NH_2. Similar behavior was seen when H_2TMPyP was loaded onto the surfaces of UiO-66 (Fig. 9c and d) and MIP-202 (Fig. 9e and f). The matching of the Q-band of the loaded photo-excited H_2TMPyP units across the surface of MOFs with the wavelength of the laser source utilized in the microscope (658 nm) may be the cause of the brightness of the self-assembled composites (Fig. S9†). A further indicator of the

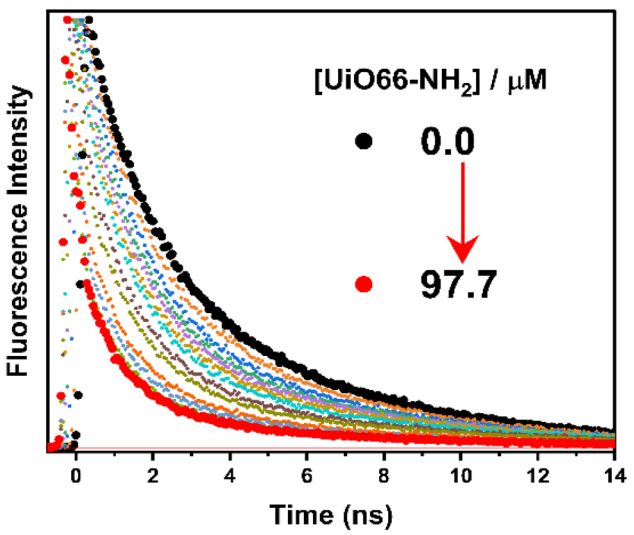

Fig. 7 TCSPC decay profiles for titration of H_2TMPyP (3.0 μM) with UiO-66 (0–97.7 μM). The excitation light was fixed at 439 nm.

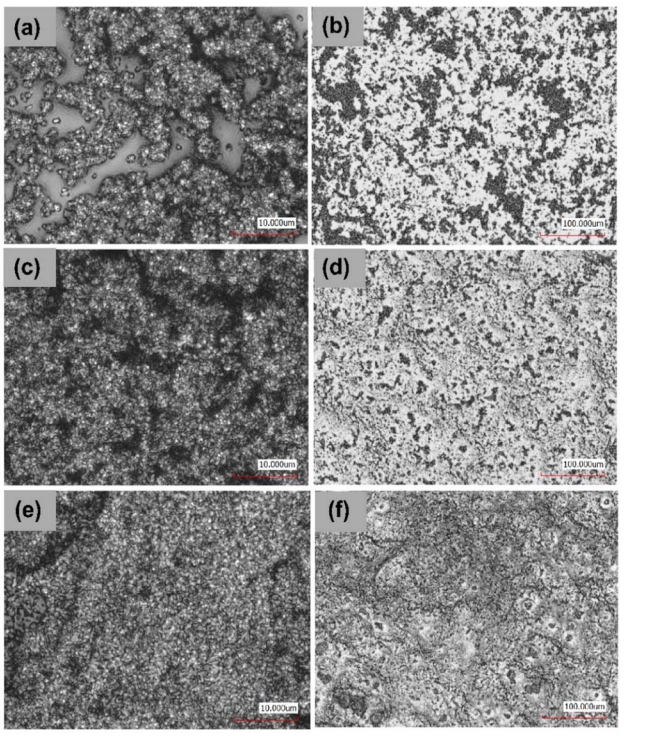

Fig. 8 Laser scanning confocal microscope images of: (a) UiO-66-NH_2, (b) H_2TMPyP@UiO-66-NH_2 complex, (c) UiO-66, (d) H_2-TMPyP@UiO-66 complex, (e) MIP-202, and (f) H_2TMPyP@MIP-202 complex.

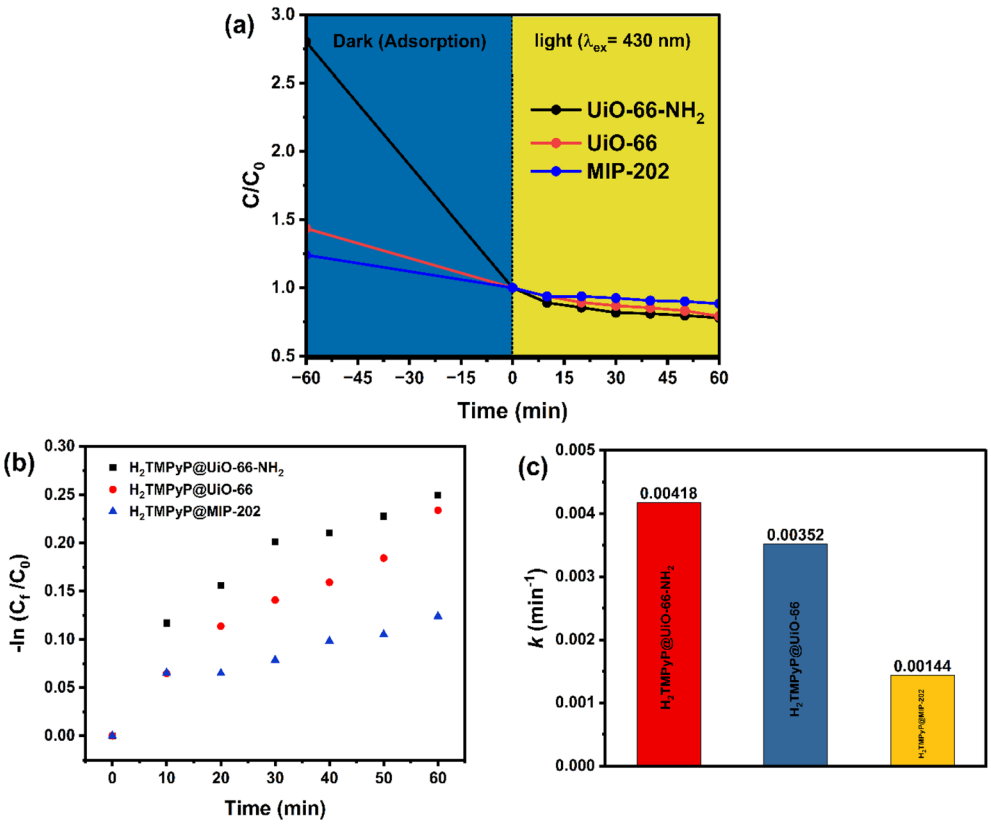

Fig. 9 (a) Rate of photodegradation of MO dye under (λ_{ex} = 430 nm) light irradiation [conditions: catalyst dosage of 10 mg, MB concentration of 20 mg L^{-1}], (b) first-order reaction kinetics of the photocatalytic degradation of MO using H_2TMPyP@MOF composites, and (c) rate constant values (k) of the photocatalytic degradation reaction of MO using H_2TMPyP@MOF composites.

increasing porphyrin loading in the samples is the observed pattern of gradual brightness increase in the three composites (H_2TMPyP@UiO-66-NH_2 > H_2TMPyP@UiO-66 > H_2-TMPyP@MIP-202), which is consistent with the aforementioned absorption and fluorescence measurements (Fig. 5–7). When porphyrin units were loaded onto the surface of GO, a similar pattern of behavior was seen.[36]

3.3. Evaluation of the photocatalytic degradation of methyl orange dye

A significant variation in the absorption capacity was indicated from the results illustrated in Fig. 9 for the three fabricated MOF composites with the UiO-66-NH_2 having the highest absorption capacity followed by UiO-66 and MIP-202 respectively. Moreover, the three MOF composites showed photocatalytic degradation efficiencies of 21.5%, 20.6%, and 11.5% for the UiO-66-NH_2, UiO-66, and MIP-202 samples, respectively, which can be elaborated in terms of the varying porphyrinic loading on the surface. In order to understand the reaction kinetics, the rate constant of the photodegradation reaction was calculated using a pseudo-first-order model (Fig. 9a) using the following equation: $k_t = -\ln(C_0/C_t)$, where (k_t) is the rate constant in min^{-1}, (t) is time in minutes, (C_0) represents the dye concentration before degradation, and (C_t) represents the dye concentration after a given amount of time (t). As seen in Fig. 9b, the rate constants for the photocatalytic degradation reactions of MO using the three MOF composites were calculated and found to be 0.0042 min^{-1} in the case of H_2-TMPyP@UiO-66-NH_2, 0.0035 min^{-1} for H_2TMPyP@UiO-66, and 0.0014 min^{-1} for H_2TMPyP@MIP-202. The values of the regression coefficients (R^2) were found to be 0.9233, 0.9406, and 0.98514 respectively. The previous findings prove that the H_2-TMPyP@UiO-66-NH_2 composite had the highest reaction rate value with a slight advantage over the H_2TMPyP@UiO-66 composite, which is in good agreement with the previously reported data.

4. Conclusion

The surface decoration of UiO-66-NH_2, UiO-66, and MIP-202 using a water-soluble porphyrin H_2TMPyP *via* post-synthetic self-assembly was investigated *via* various spectroscopic and microscopic techniques. The loading of H_2TMPyP and the stability of the three composites were found to be significantly dependent on the type of targeted non-covalent interactions with the linker as observed from the laser fluorescence images, as well as the steady-state absorption and fluorescence measurements. The BET results showed a high surface area and pore volume of UiO-66 (1100 m^2 g^{-1} and 0.6834 cm^3 g^{-1}) compared to that of MIP-202 (surface area = 94 m^2 g^{-1} and pore volume = 94 cm^3 g^{-1}). Keeping into consideration the large

diameter of the porphyrin molecule (approximately 0.26 nm) along with the low pore diameter of the three MOFs confirms the presence of the H_2TMPyP on the surface. Also, a comparative study on the photocatalytic degradation of Methyl orange dye from aqueous solution using the three composites was conducted under visible light using a continuous-flow reactor at room temperature. The photocatalytic degradation efficiencies were found to be directly proportional to the porphyrinic loading on the surface of the three MOFs.

Conflicts of interest

The authors declare no conflict of interest.

References

1 X. Yang and D. Wang, Photocatalysis: From Fundamental Principles to Materials and Applications, *ACS Appl. Energy Mater.*, 2018, **1**(12), 6657–6693.
2 S. Fukuzumi, *Electron Transfer: Mechanisms and Applications*, Wiley-VCH, 2020.
3 S. Navalón, A. Dhakshinamoorthy, M. Álvaro, B. Ferrer and H. García, Metal–Organic Frameworks as Photocatalysts for Solar-Driven Overall Water Splitting, *Chem. Rev.*, 2022, **123**(1), 445–490.
4 C. Lin, C. Han, H. Zhang, L. Gong, Y. Gao, H. Wang, Y. Bian, R. Li and J. Jiang, Porphyrin-Based Metal–Organic Frameworks for Efficient Photocatalytic H_2 Production under Visible-Light Irradiation, *Inorg. Chem.*, 2021, **60**(6), 3988–3995.
5 C. Wu and M. Zhao, Incorporation of Molecular Catalysts in Metal–Organic Frameworks for Highly Efficient Heterogeneous Catalysis, *Adv. Mater.*, 2017, **29**, 1605446.
6 L. Zeng, X. Guo, C. He and C. Duan, Metal–Organic Frameworks: Versatile Materials for Heterogeneous Photocatalysis, *ACS Catal.*, 2016, **6**(11), 7935–7947.
7 W. Chen, Y. Zhuang, L. Wang, Y. Lv, J. Liu, T. L. Zhou and R. J. Xie, Color-Tunable and High-Efficiency Dye-Encapsulated Metal-Organic Framework Composites Used for Smart White-Light-Emitting Diodes, *ACS Appl. Mater. Interfaces*, 2018, **10**(22), 18910–18917.
8 L. Wang, H. Fan and F. Bai, Porphyrin-based photocatalysts for hydrogen production, *MRS Bull.*, 2020, **45**, 49–56.
9 K. Rybicka-Jasińska, T. Wdowik, K. Łuczak, A. J. Wierzba, O. Drapała and D. Gryko, Porphyrins as Promising Photocatalysts for Red-Light-Induced Functionalizations of Biomolecules, *ACS Org. Inorg. Au*, 2022, **2**, 422–426.
10 W. Zhu, N. Sharma, Y.-M. Lee, M. E. El-Khouly, S. Fukuzumi and W. Nam, Use of singlet oxygen in the generation of a mononuclear nonheme iron(IV)-Oxo complex, *Inorg. Chem.*, 2023, **62**(10), 4116–4123.
11 N. Sharma, J. jieun, K. Ohkubo, L. Ying-Min, M. E. El-Khouly, W. Nam and S. Fukuzumi, Long-lived photoexcited state of a Mn(IV)-Oxo complex binding scandium ions that is capable of hydroxylation benzene, *J. Am. Chem. Soc.*, 2018, **140**(27), 8405–8409.
12 A. E. O'Connor, W. M. Gallagher and A. T. Byrne, Porphyrin and Nonporphyrin Photosensitizers in Oncology: Preclinical and Clinical Advances in Photodynamic Therapy, *Photochem. Photobiol.*, 2009, **85**(5), 1053–1074.
13 R. R. Cheruku, J. Cacaccio, F. A. Durrani, W. A. Tabaczynski, R. Watson, A. Marko, R. Kumar, M. E. El-Khouly, S. Fukuzumi, J. R. Missert, R. Yao, M. Sajjad, D. Chandra, K. Guru and R. K. Pandey, Epidermal growth factor receptor-targeted multifunctional photosensitizers for bladder cancer imaging and photodynamic therapy, *J. Med. Chem.*, 2019, **62**(5), 2598–2617.
14 J. Chen, Y. Zhu and S. Kaskel, Porphyrin-Based Metal–Organic Frameworks for Biomedical Applications, *Angew. Chem., Int. Ed.*, 2021, **60**, 5010–5035.
15 M. H. Alkordi, Y. Liu, R. W. Larsen, J. F. Eubank and M. Eddaoudi, Zeolite-like Metal−Organic Frameworks as Platforms for Applications: On Metalloporphyrin-Based Catalysts, *J. Am. Chem. Soc.*, 2008, **130**(38), 12639–12641.
16 N. Rabiee, M. Rabiee, S. Sojdeh, Y. Fatahi, R. Dinarvand, M. Safarkhani, S. Ahmadi, H. Daneshgar, F. Radmanesh, S. Maghsoudi, M. Bagherzadeh, R. S. Varma and E. Mostafavi, Porphyrin Molecules Decorated on Metal–Organic Frameworks for Multi-Functional Biomedical Applications, *Biomolecules*, 2021, **11**(11), 1714.
17 J. L. Kan, Y. Jiang, A. Xue, Y. H. Yu, Q. Wang, Y. Zhou and Y. B. Dong, Surface Decorated Porphyrinic Nanoscale Metal-Organic Framework for Photodynamic Therapy, *Inorg. Chem.*, 2018, **57**(9), 5420–5428.
18 S. Wang, W. Morris, Y. Liu, C. M. McGuik, Y. Zhou, J. T. Hupp, O. K. Farha and C. A. Mirkin, Surface specific functionalization of nanoscale metal-organic frameworks, *Angew. Chem., Int. Ed.*, 2015, **54**, 14738–14762.
19 K. E. Diab, E. Salama, H. S. Hassan, A. Abd El-Moneim and M. F. Elkady, Biocompatible MIP-202 Zr-MOF Tunable Sorbent for Cost-Effective Decontamination of Anionic and Cationic Pollutants from Waste Solutions, *Sci. Rep.*, 2021, **11**, 6619.
20 K. Safo, H. Noby, M. Matatoshi, H. Naragino and A. H. Shazly, Statistical optimization modeling of organic dye photodegradation process using slag nanocomposite, *Res. Chem. Intermed.*, 2022, **48**(10), 4183–4208.
21 W. Chen, Y. Zhuang, L. Wang, Y. Lv, J. Liu, T. L. Zhou and R. J. Xie, Color-Tunable and High-Efficiency Dye-Encapsulated Metal-Organic Framework Composites Used for Smart White-Light-Emitting Diodes, *ACS Appl. Mater. Interfaces*, 2018, **10**(22), 18910–18917.
22 M. He, J. Zhou, J. Chen, F. Zheng, D. Wang, R. Shi, Z. Guo, H. Wang and Q. Chen, Fe_3O_4@carbon@zeolitic Imidazolate Framework-8 Nanoparticles as Multifunctional pH-Responsive Drug Delivery Vehicles for Tumor Therapy in vivo, *J. Mater. Chem. B*, 2015, **3**(46), 9033–9042.
23 Y. Cao, H. Zhang, F. Song, T. Hunag, J. Ji, Q. Zhong, W. Chu and Q. Xu, UiO-66-NH_2/GO composite: Synthesis, characterization and CO_2 adsorption performance, *Materials*, 2018, **11**(4), 589.
24 Z. Li, T. M. Rayder, L. Luo, J. Byers and C.-K. Tsung, Aperture-Opening Encapsulation of a Transition Metal Catalyst in

a Metal–Organic Framework for CO_2 Hydrogenation, *J. Am. Chem. Soc.*, 2018, **140**(26), 8082–8085.

25 J. V. Morabito, L.-Y. Chou, Z. Li, C. M. Manna, C. A. Petroff, R. J. Kyada, J. M. Palomba, J. A. Byers and C.-K. Tsung, Molecular Encapsulation beyond the Aperture Size Limit through Dissociative Linker Exchange in Metal–Organic Framework Crystals, *J. Am. Chem. Soc.*, 2014, **136**(36), 12540–12543.

26 R. X. Wang, J. J. Fan, Y. J. Fan, J. P. Zhong, L. Wang, S. G. Sun and X. C. Shen, Platinum Nanoparticles on porphyrin functionalized graphene nanosheets as superior catalysts for methanol electrooxidation, *Nanoscale*, 2014, **6**(24), 14999–15007.

27 D. Lozano-López, M. Galván-Valencia, I. Rojas-de Soto, R. A. Escalona-Villalpando, J. Ledesma-García and S. Durón-Torres, Immobilization of Glucose Oxidase on Glutathione Capped CdTe Quantum Dots for Bioenergy Generation, *Catalysts*, 2022, **12**(12), 1659.

28 J. Zhu, L. Wu, Z. Bu, S. Jie and B. G. Li, Polyethyleneimine-Modified UiO-66-NH_2(Zr) Metal-Organic Frameworks: Preparation and Enhanced CO_2 Selective Adsorption, *ACS Omega*, 2019, **4**(2), 3188–3197.

29 L. Valenzano, B. Civalleri, S. Chavan, S. Bordiga, M. H. Nilsen, S. Jakobsen, K. P. Lillerud and C. Lamberti, Disclosing the Complex Structure of UiO-66 Metal Organic Framework: A Synergic Combination of Experiment and Theory, *Chem. Mater.*, 2011, **23**(7), 1700–1718.

30 Y. Fang, L. Zhang, Q. Zhao, X. Wang and X. Jia, Highly Selective Visible-Light Photocatalytic Benzene Hydroxylation to Phenol Using a New Heterogeneous Photocatalyst UiO-66-NH_2-SA-V, *Catal. Lett.*, 2019, **149**(9), 2408–2414.

31 H. A. Benesi and J. H. Hildebrand, A spectrophotometric investigation of the interaction of iodine with aromatic hydrocarbons, *J. Am. Chem. Soc.*, 2002, **71**, 2703–2707.

32 R. Teixeira, V. V. Serra, P. M. R. Paulo, S. M. Andrade and S. M. B. Costa, Encapsulation of Photoactive Porphyrinoids in Polyelectrolyte Hollow Microcapsules Viewed by Fluorescence Lifetime Imaging Microscopy (FLIM), *RSC Adv.*, 2015, **5**(96), 79050–79060.

33 Y. Xu, L. Zhao, H. Bai, W. Hong, C. Li and G. Shi, Chemically Converted Graphene Induced Molecular Flattening of 5,10,15,20-Tetrakis(1-Methyl-4-Pyridinio)Porphyrin and Its Application for Optical Detection of Cadmium(II) Ions, *J. Am. Chem. Soc.*, 2009, **131**(37), 13490–13497.

34 Z. Chernia and D. Gill, Flattening of TMPyP Adsorbed on Laponite. Evidence in Observed and Calculated UV-vis Spectra, *Langmuir*, 1999, **15**(5), 1625–1633.

35 The quenching rate, as well as the mechanism of quenching, can be derived using the Stern–Volmer equation: $F_0/F = 1 + K_q\tau_0[Q] = 1 + K_{SV}[Q]$, where F_0 is the fluorescence before quenching, F is the fluorescence after adding the quencher, $[Q]$ represents the concentration of the quencher, K_{SV} is the Stern–Volmer constant, K_q is the bimolecular quenching rate and τ_0 is the fluorescence lifetime before quenching. By plotting F_0/F against $[Q]$ we could obtain three linear Stern–Volmer plots with different slopes for the three complexes (Fig. 7d). The linear plots suggest that the main quenching mechanism is complex formation.

36 N. El-Shafai, M. E. El-Khouly, M. El-Kemary, M. S. Ramadan and M. S. Masoud, Self-Assembly of Porphyrin on Graphene Oxide in Aqueous Medium: Fabrication, Characterization, and Photocatalytic Studies, *Photochem. Photobiol. Sci.*, 2019, **18**(8), 2071–2079.